Cyclic voltammetry and high-frequency series resistance of La0.6Sr0.4Co0.2Fe0.8O3-δ electrode deposited on GDC : effect of the electrode microstructure and the oxygen partial pressure

V. Tezyk, C. Rossignol, N. Sergent, Elisabeth Djurado, Jérôme Laurencin, Elisabeth Siebert

Cyclic voltammetry and high-frequency series resistance of $La_{0.6}Sr_{0.4}Co_{0.2}Fe_{0.8}O_{3-\delta}$ electrode deposited on GDC : effect of the electrode microstructure and the oxygen partial pressure.

V. Tezyk [(a)], C. Rossignol [(a)], N. Sergent [(a)], E. Djurado [(a)], J. Laurencin [(b)], E. Siebert [(a*)]

[(a)] Univ. Grenoble Alpes , Univ. Savoie Mont Blanc, CNRS, Grenoble INP, LEPMI, 38000 Grenoble, France

[(b)] Univ. Grenoble Alpes – CEA/LITEN, 17 rue des Martyrs, 38054, Grenoble, France

Abstract

$La_{0.6}Sr_{0.4}Co_{0.2}Fe_{0.8}O_{3-\delta}$ (LSCF) electrode deposited on Gadolinium Doped Ceria (GDC) has been characterized by cyclic voltammetry and impedance spectroscopy in the temperature range of 300 to 700 °C. We demonstrate that the LSCF microstructure has a strong influence on the shape of the voltammograms and on the variation of the series resistance, R_s, measured on the impedance diagrams as a function of the dc bias. LSCF was deposited with two different microstructures, either porous layer (~10 µm thick) by screen-printing (SP) or almost dense layer (~2 µm thick) by Electrostatic Spray Deposition (ESD). For the denser film, one cathodic peak and one reverse anodic peak were evidenced under air at 300 and 500°C. The R_s value was also found to increase with the dc cathodic bias. On the contrary, no peak was observed with the porous film under the same conditions and R_s was independent on the applied potential from 300 to 700°C. Decreasing the oxygen partial pressure allowed the peaks to be evidenced and R_s to vary. The results are discussed in terms of oxygen exchange rate at the LSCF/gas interface, which depends on the LSCF specific surface area and the oxygen partial pressure.

Keywords: LSCF/GDC interface, cyclic voltammetry, high-frequency series resistance, microstructure, oxygen partial pressure

* Corresponding author :

E-mail address : Elisabeth.siebert@lepmi.grenoble-inp.fr

Address : LEPMI – 1130 rue de la piscine – BP 75 - 38402 Saint Martin d'Hères cedex – France

1. Introduction

$La_{1-x}Sr_xCo_yFe_{1-y}O_{3-\delta}$ perovskite oxides are good candidates for oxygen electrode materials in Solid Oxide Fuel Cells (SOFC) and Solid Oxide Electrolysis Cells (SOEC) operating at intermediate temperatures (500-800°C) [1]. In particular, the composition $La_{0.6}Sr_{0.4}Co_{0.2}Fe_{0.8}O_{3-\delta}$ (LSCF) in contact with Gadolinium Doped Ceria (GDC) is widely accepted as the oxygen electrode material with a good trade-off between electrochemical performances and long-term stability. Indeed, this compound exhibits suitable electronic and ionic conductivity [2–5] leading to good electrochemical performances [6–10]. Concerning the electrolyte, GDC is preferred to the standard Yttria Stabilized Zirconia (YSZ) electrolyte in order to avoid the reactivity of LSCF at high temperature with YSZ, which results in the formation of insulating phases at the interface [11]. Kharton et al. [12] reported the best stability for 10 mol. % Gd-doped ceria ($Ce_{0.9}Gd_{0.1}O_{2-\delta}$) in reducing atmospheres and at temperatures below 1000 K, which makes $Ce_{0.9}Gd_{0.1}O_{2-\delta}$ the most appropriate electrolyte material for IT-SOCs. In addition, the linear thermal expansion coefficient of $Ce_{0.9}Gd_{0.1}O_{2-\delta}$ in the temperature range of 30 to 800 °C is equal to $\alpha_{GDC} = 13.4 \cdot 10^{-6}$ K^{-1} which is close to LSCF [2]. This good compatibility improves the long-term stability of solid oxide cells [13].

The electrochemical properties of the LSCF/GDC electrode are related to the degree of the oxygen deficiency within LSCF which is strongly dependent on the B site ion oxidation state within perovskite type ABO_3 metal oxides at high temperature [14]. High concentration of oxygen vacancies leads to high oxygen reduction rate, thus increasing the performance of LSCF as cathode. However, high oxygen vacancy content can affect the structural stability of LSCF [15] and its thermochemical stability [16]. Those properties are also highly dependent on the redox properties of the B site [17].

Cyclic voltammetry has already been used to characterize the reducibility of the B site and formation of oxygen vacancies [18–20]. Previous studies of the porous Co-rich compound, $La_{0.7}Sr_{0.3}Co_{0.8}Fe_{0.2}O_{3-\delta}$, deposited on GDC have been carried out by cyclic voltammetry [21] and

Raman spectroscopy measurements, from 300 to 500 °C, under applied dc voltage [22]. A reversible phase transition from perovskite (ABO_3) towards the brownmillerite ($ABO_{2.5}$ or $A_2B_2O_5$) was observed under cathodic polarization leading to the existence of two cathodic peaks on the voltammograms under air. The cathodic peaks were tentatively attributed to the reduction of Co^{4+} to Co^{2+} in tetrahedral environment. On the contrary, for the porous Fe-rich $La_{0.8}Sr_{0.2}Co_{0..2}Fe_{0.8}O_{3-\delta}$ compound, Kournoutis et al. [23] have concluded that no peak was observed under air in the temperature range of 600 to 800 °C. However, when the oxygen partial pressure was decreased, current peaks appeared both in the forward and backward scans.

In the present work, LSCF deposited on GDC was studied by cyclic voltammetry and dc bias impedance measurements over a wide range of temperatures and oxygen partial pressures. LSCF was deposited with two different microstructures: (i) porous 10 µm thick film prepared by Screen-Printing (SP) and (ii) almost dense 2 µm thin film deposited by Electrostatic Spray Deposition (ESD) [10]. The purpose of the study was to understand the role of the microstructure and the oxygen partial pressure on the shape of the voltammograms and the variation of the series resistance, R_s, deduced from the high-frequency axis intercept on the impedance diagrams as a function of the dc bias.

2. Experimental

2.1. Sample preparation

The dense $Ce_{0.9}Gd_{0.1}O_{2-\delta}$ substrate, ≈ 1 mm in thickness, was prepared by isostatically pressing of GDC powder (Praxair, 99.9 %, 20.5 $m^2.g^{-1}$) at 300 MPa, followed by sintering at 1200 °C for 2 h in air. The substrates were polished with abrasive disc P400, on MECAPOL P 200 machine, in order to obtain a flat and uniform surface, allowing a well-defined and reproducible surface for further deposits.

The starting $La_{0.6}Sr_{0.4}Co_{0.2}Fe_{0.8}O_{3-\delta}$ commercial powder was provided from Marion Technologies with particle size distribution d_{50} = 0.27 µm. Porous LSCF electrodes were deposited by screen-printing. The ink was made-up by mixing LSCF powder with a commercial solvent "Product KD2921" (ZSCHIMMER & SCHWARZ) 50/50 wt. % and 2 % total weight polymer PVB (Polyvinyl butyral) as binder. A printing screen with a very fine mesh (INOX MESH SD 95/46) was used. The screen-printed sample was pre-annealed at 450 °C (heating rate 1 °C.min^{-1}) to burn out binders and ink solvents. Then, it was fired at 900 °C for 2 hours in air (heating rate 2 °C.min^{-1}) to get good adhesion on GDC. It is worth mentioning that this heat treatment takes place at a lower temperature than that conventionally used for the deposit of LSCF by SP [23]. Consequently, possible changes in the electrode microstructure cannot be excluded because the electrode is likely to be less stable than the conventional electrode.

An almost dense electrode was deposited by ESD as described in [10]. It will be denoted "dense" throughout the text. A precursor salt solution was prepared by weighing $La(NO_3)_3.6H_2O$ (Prolabo, 99.99%), $SrCl_2.6H_2O$ (Strem Chemicals, 99%), $Co(NO_3)_2.6H_2O$ (Sigma-Aldrich, 99.999%) and $Fe(NO3)_2.9H_2O$ (Sigma-Aldrich, 99.99%) salts in adequate amounts, as to obtain the $La_{0.6}Sr_{0.4}Co_{0.2}Fe_{0.8}O_{3-\delta}$ composition. The solution was obtained by mixing salts in ethanol (C_2H_5OH, 99.9%; Prolabo) and diethylene glycol monobutyl ether, also known as butyl carbitol $CH_3(CH_2)_3OCH_2CH_2OCH_2CH_2OH$ (Acros Organics, 99+%) with a 1:2 volume ratio. Depositions were made at 30 mm nozzle-to-substrate distance and 1.59 mL h^{-1} solution flow rate, using a model A-99 Bioblock Scientific flowmeter. Deposition time was equal to 3 h. The substrate temperature was 300 °C with a value referring to the surface of the substrate facing the solution spray, obtained after temperature calibration. A positive voltage ranging from 8 to 10 kV was selected and applied between the nozzle and the grounded substrate for aerosol generation and spray stabilization. The sample was annealed at 900 °C in air for 2 h. ESD was also used to prepare a porous sample with a columnar microstructure. The sample was deposited in the conditions depicted in [10] but with a deposition time equal to 6 h.

For all the films, X-ray diffraction showed that the LSCF exhibited a single rhombohedral phase with $R\bar{3}c$ space group.

2.2. Microstructure characterization

The characterization of the LSCF microstructure was performed by Scanning Electron Microscopy (SEM) with a field emission gun equipment (ZEISS Ultra 55), operating at 3-10 kV voltage and 6.4-7 mm working distance. The samples were coated with Pt to avoid electron charging. The samples were analyzed on the surface as well as on a fresh fractured section. For the porous sample, the average grain and pore sizes, as well as the porosity, were estimated using the ImageJ software. This analysis was performed on a polished LSCF surface.

2.3. Electrochemical measurements

The electrochemical measurements were performed with a three-electrode set-up. The geometry and nature of the electrodes are depicted in Fig. 1. For characterization of porous SP layer, both working and counter electrodes, WE and CE respectively, were deposited symmetrically on each side of the electrolyte (surface area ≈ 1.1 cm²). For characterization of dense and thin LSCF, the counter electrode consisted of a silver paste (Ferro L-200N) deposited symmetrically with the LSCF working electrode (surface area ≈ 0.5 cm^2). In both set-ups, the reference electrode (RE) consisted of an Ag wire applied on the periphery of the GDC pellet, in the middle of the cylinder height. This geometry ensured a rather uniform current density through the cell, thus solving the problem in solid-state electrochemistry with the position of the reference electrode [24]. Ag was used instead of Pt because it is a better oxygen reference electrode at low temperature. Indeed, the Nernst law is well verified for the reference electrode by using this material even at T<500°C. Gold grids with a surface area equal to that of LSCF electrodes were used as current

collectors (fine 52 mesh woven from 0.102 Alfa Aesar). The electrical contact between gold grids and the sample was ensured by mechanical pressure. The electrochemical measurements were performed from 300 to 700 °C for the porous sample, in order to be as close as possible to the conditions of SOFC and/or SOEC. For the dense sample, only two temperatures were characterized, i.e. 300 and 500°C. The gas flow was synthetic O_2 + N_2 gas mixture or Ar, with 3 $L.h^{-1}$ flow rate. The oxygen partial pressure within the gas was measured with an oxygen gauge located at the exit of the furnace. The oxygen gauge was a home-made potentiometric sensor based on yttria stabilized zirconia. It used ambient air as reference atmosphere and was operating at 700°C.

The electrochemical measurements were performed with a Solartron SI 1280B electrochemical equipment. Electrochemical impedance measurements at Open-Circuit Voltage (OCV) were first measured as a function of temperature, in order to check the reproducibility of the electrode and evaluate the precision of the measurement. They were carried out with an ac signal amplitude of 50 mV, over a frequency range of 20 kHz to 0.5 Hz. Impedance spectra were fitted with electrical circuits using the EC-Lab® software (V11.01) as described in our previous work [25]. This allowed the determination of the ohmic series resistance, R_s, corresponding to the high-frequency intercept with the real axis, the electrode polarization resistance, R_{pol}, determined from the low-frequency intercept, and the top impedance diagram frequency, f_0, as defined in Fig. 2a. This figure shows a typical impedance spectrum recorded at OCV. As expected from our previous work [25] and from literature data [26], the classical Gerischer impedance is obtained at 500°C, for the porous film. As a consequence, the frequency, f_0, can be linked to the characteristic time constant, t_{chem}, defined by ALS model [26] according to:

$$f_0 = \frac{\sqrt{3}}{2\pi t_{chem}} \quad (1)$$

with $t_{chem} \propto 1/S_{MIEC}/gas$, where S_{MIEC}/gas is the LSCF specific surface area. It is worth mentioning that the impedance diagram shape changes from the Gerischer-type element (Ge), corresponding to a semi-infinite medium, to the finite-length Gerischer element (FLGe) when the thickness of the electrode decreases and/or the gas exposed surface area decreases [27]. The finite-length-Gerischer

impedance starts with the Warburg impedance at high frequencies and turns into a semi-circle at low frequencies. In that case, the relationship between f_0 and t_{chem} must diverge from Eq. (1). However, whatever the Ge or LFGe behavior, the value of the characteristic frequency f_0, defined as the maximum absolute value of the imaginary part of the impedance, exhibits the same dependence with the gas/LSCF interfacial specific surface area.

The error on R_s, R_{pol} and f_0 was estimated from measurements on 4 similar porous samples. The Arrhenius plot of R_s (Fig. 2b) shows that the error was small (less than ±0.05) at low temperature while it increased at high temperature (T > 490 °C). It was estimated to be ±0.07 on a logarithmic scale. This larger error could be explained by the decrease of ohmic resistance of the cell with increasing the temperature so that the contribution of the contact resistance (roughly independent of T) induced the scattering in R_s. Moreover, the identification error on R_s became more important as the temperature increased due both to the smaller value of R_s and the more pronounced high-frequency artifacts. For log (R_{pol}) (Fig. 2c), the error was constant on the whole temperature range. It was equal to ±0.11. This dispersion was mainly attributed to difference in porous film reproducibility during the synthesis process. By assuming that the error at OCV was the same as under dc polarization, it could be suggested that the error on the logarithm of the faradaic current would be equal to ±0.11. This value will be used on the polarization curve Tafel plot. In the same way as R_{pol}, the error on log (f_0) (Fig. 2d) was found to be independent of the temperature and equal to ±0.1. This led to $\Delta f_0 / f_0 = \pm 0.1$ corresponding to an error of ±10% on f_0. Thereafter, f_0 will be used to compare S_{MIEC}/gas for the different samples tested. Therefore, samples will be considered to have a specific surface area variation if the difference between f_0 is greater than 20%.

Then, the polarization curves, as well as the impedance diagrams under polarization, were recorded using the up-face as the working electrode. The polarization curve was measured in a potentiostatic mode with a potential step of 50 mV. The applied potential, denoted E, varied in the range of 0.3 to -0.7 V. The equilibration time was equal to 600 s as shown by the corresponding chronoamperometric curves (I *vs* t), which were recorded to check the stationarity of the current. The dc impedance spectra were recorded at each applied potential with the same ac signal

amplitude than the one used at OCV. In the present work, we were interested in the variation of R_s with dc potential, denoted $R_s(E)$. The R_{pol} dependence on the polarization was reported in a recent previous work [25]. In the present work, the polarization curves were presented as log (j) *vs* η, where η was the overvoltage, corresponding to the applied potential corrected from the ohmic drop according to:

$$\eta = E - Rs(E).j(E) \quad (2)$$

In Eq. (2), j(E) was the current density calculated from the geometric surface area of the LSCF layer and $R_s(E)$ was the potential dependent series resistance.

The linear sweep cyclic voltammetry experiments were performed by varying linearly the electrode potential with scan rates, v, in the range from 0.5 $mV.s^{-1}$ to 500 $mV.s^{-1}$. An anodic pretreatment, 0.1 V/air during 20 min, was applied to stabilize the same oxidation state of the electrodes corresponding to a low oxygen vacancy concentration within LSCF ($\delta \rightarrow 0$). In the present paper, the potential on the voltammograms was the potential uncorrected from the ohmic drops. As it corresponded to the applied potential, it was denoted E by analogy with the terminology of Eq. (2). The peak potential, η_p, was determined from E by correction from the ohmic drop and calculated with respect to 1 atm of oxygen according to the Nernst equation expressed as:

$$\eta_p(V_{/\,1\,atm}) = \eta(V_{/x\,atm}) + \frac{RT}{4\mathcal{F}}\ln(x) \quad (3)$$

where x was the corresponding pO_2 atmosphere. This was done in order to keep the same potential scale and to be able to compare the results obtained under different pO_2.

The open-circuit potential was measured before each experiment and, as expected, was practically zero.

3. Results

3.1. Role of the microstructure

The study on the role of the microstructure on electrochemical properties was performed under pO_2 = 0.21 atm, by comparing the response of a porous and a dense film. Fig. 3 presents surface and cross-sectional SEM images for the different electrode microstructures tested in the present work. The micrograph in Fig. 3b shows that the porous film prepared by SP was 10 µm thick. It was homogeneous and uniform over the whole section. The average particle and pore sizes were almost the same (see Table 1) and around 90 nm, which corresponded to a rather fine microstructure. This result could be related to the low sintering temperature [27,28]. The porosity was equal to 43 ± 2%. A good adherence between the electrode and the electrolyte was obtained. Fig. 3c and 3d give the surface and cross-sectional SEM images of the dense LSCF layer prepared by ESD. The film thickness was lower and equal to ~2 µm. The electrode presented a good adherence to the electrolyte and the microstructure was homogeneous. Some closed and open porosities at the nanoscale were evidenced as already shown by Marinha et al. [10]. However, the open porosity was very low as evidenced by the surface image, which presented very few pores in comparison to the porous sample. It can be noticed that the so-called dense film could be rather considered as nanoporous in comparison with dense films deposited by Pulsed Laser Deposition (PLD) [31]. Taking into account the values of f_0 given in Table 1, it can be proposed that the dense film has a very small specific surface area compared to the porous film.

Table 1

f_0 and diagram shape (Ge = Gerischer-type, FLGe = finite-length-Gerischer-type) measured at T = 500°C and PO_2 = 0.21 atm for the different films tested in the present work. Microstructure parameters determined from image analysis on the porous sample.

	f_0, Hz	Diagram Shape	Porosity, %	Particle size, µm	Pore size, µm
Porous	26 ± 3	Ge	43±2	0.09	0.09
Dense	$<10^{-1}$	FLGe	N/A	N/A	N/A
Columnar	2	Ge	-	-	-

Fig. 4a shows the typical voltammetry response corresponding to the porous LSCF electrode. No peaks were evidenced and the cyclic voltammetry corresponded to the steady-state polarization curve. This shape was obtained whatever the scan rate, v, from 0.5 to 500 $mV.s^{-1}$ in the whole temperature range (from 300 to 700 °C). This result is in good agreement with the study of Kournoutis et al. [23], who have not detected any peak under air. However, no reverse hysteresis was observed in the backward scan in our work, while Kournoutis et al. [23] have highlighted this phenomenon, corresponding to higher currents in the backward scan than in the forward scan. Fig. 4b represents the R_s *vs* E curve measured at different temperatures. The upper limit of 550°C, chosen to present the results was due to the fact that, above 600°C, impedance diagrams under dc bias may have high-frequency artifacts, that make it difficult to determine R_s accurately. However, despite the dispersion of the experimental points, the results obtained at 600 and 700°C on one sample confirm the evolution trend observed from 300 to 550°C on all the samples. Based on this comment and on the results in Fig. 4a, it can be concluded that R_s was independent on the applied potential whatever the temperature from 300 to 700°C. The series resistance, R_s, is commonly associated with the migration of O^{2-} ions through the electrolyte. Comparison with literature data and, in particular, R_s^{GDC} calculated from the GDC conductivity reported by Steele [29], shows that the measured R_s was slightly higher than the theoretical resistance R_s^{GDC}, roughly estimated from a 1D geometry with a thickness equal to half that of the GDC pellet and a surface area equal to that of LSCF. Moreover, the activation energy for OCV conditions measured from all tested samples was between 0.5 and 0.55 eV. This value was lower than the value of 0.64 eV given by Steele [29] for T > 400°C. The difference between R_s and R_s^{GDC} increased when the temperature was increased. This phenomenon was already observed in our previous work [21]. The difference between both sets of data might be attributed to small differences in sample composition and/or bad current collector properties due to an electrical sheet resistance of the porous LSCF electrode [30]. This effect could be reinforced at high temperature as the electrical conductivity of LSCF decreases with increasing the temperature above 500°C [2]. Moreover, as already stated in the experimental

section, additional contact resistance due to the experimental set-up may also lead to an error on the value of R_s measured at high temperature.

Fig. 5a shows the typical voltammetry response for dense LSCF obtained at 500 °C. One cathodic peak corresponding to the forward scan (from 0.1 to -1 V) and a reverse anodic peak corresponding to the backward scan (from -1 to 0.1 V) were observed. The cathodic and anodic peaks were almost of the same shape from 2 to 160 $mV.s^{-1}$, with approximately the same surface area at 300°C. As expected, the peak intensities were increasing with the scan rate. Indeed, the ratio between the current and the scan rate (I/v) corresponds to the capacitance in a charge/discharge process. The R_s *vs* E curve is given in Fig. 5b. Contrary to the porous sample, R_s was found to rise with the applied cathodic potential. The polarization threshold at which R_s started to increase was shifted toward more cathodic overpotential when temperature was decreased. Indeed, the overpotential threshold was calculated and found to be equal to -0.28 $V_{/1\ atm}$ and -0.11 $V_{/1\ atm}$ at 300 and 500°C, respectively. For example, such R_s shift to higher values for larger cathodic dc bias have already been observed by Baumann et al. [32] on microelectrodes of the Co-rich LSCF deposited by PLD. This phenomenon was explained by decreasing of LSCF conductivity and increasing of oxygen vacancies concentration under cathodic polarization as described in [33]. As before, the value of R_s was compared to R_s^{GDC} calculated from GDC conductivity reported by Steele [29]. At 300°C, the relative difference between both sets of data was practically the same for both the porous and dense samples. However at 500°C, R_s near OCV was greatly higher than R_s^{GDC}, contrary to the porous thick film. This could be attributed to constriction phenomenon as the film thickness was only 2 µm and not thick enough for good current collecting with grids [34–36]. Actually, the LSCF electronic conductivity decreases when the concentration of oxygen vacancies $V_O^{\cdot\cdot}$ increases. So, constriction phenomenon due to in-plane resistance becomes more important under reducing conditions thus leading to $R_s >> R_s^{GDC}$ under cathodic polarization.

The effect of the sweep rate on the voltammograms was addressed by determining the variation of the peak potential, η_p, and the peak current, I_p (or peak current density, j_p). The peak potentials E_{pc} and E_{pa} were determined as represented in Fig. 6a. The cathodic peak current, I_{pc},

corresponded to the current measured at the minimum of the voltammetry response, as classically defined in electrochemistry [37, 38]. On the other hand, the determination of the reverse anodic peak current, I_{pa}, required a baseline correction as it may depend on the return potential. The baseline for I_{pa} measurement in the cathodic zone was determined as proposed by Bard and Faulkner [37], by extrapolating the limiting current in the voltammograms . It is worth mentioning that there is no solid theory behind baseline correction. In the anodic part, it was taken as the stationary current corresponding to the oxygen evolution. Indeed, this one corresponds to the surface path that takes place in parallel as shown in [39]. It should be noted that, by doing so, the baseline and dc polarization curve were almost the same. Moreover, baseline correction was necessary only for small I_{pa} or high E_{pa} values. The peak potential, η_p, was calculated from E_p, by ohmic correction according to Eq. (2), using either R_s (OCV) as it was done in our previous work [21] or R_s (E_p), *i.e.* R_s value corresponding to $E = E_p$. Fig. 6b shows an example of a result for the cathodic peak potential. The representation mode as a function of log ($v^{1/2}$) is the one proposed by Diard et al. [38]. Note that the usual scale using log (v) is obtained simply by setting log ($v^{1/2}$) = ½ log (v). The determination of η_{pc} using the ohmic drop measured at OCV led to a variation curve as a function of the scan rate similar to that observed in our previous work [21]. Indeed, η_{pc} was constant at a low scan rate and found to decrease as log (v) at the high scan rate. On the contrary, the correction by R_s (E_p) led to a strong increase of η_p at high scan rate. This huge enhancement was meaningless due to excess ohmic drop correction. This result clearly indicates that, when η_p is located in a potential zone where R_s may vary, any variation of η_p with the scan rate is rather an artifact due to the fact that the R_s value necessary for ohmic drop correction is between R_s (OCV) and R_s (E_p). In other words, the electrode series resistance R_s obtained at steady-state potential equal to the peak potential is different from the value determined at the same potential under the transient conditions of the voltammetric scan, the latter being lower but higher than the R_s under OCV. In addition, it must be emphasized that this R_s value may vary throughout the scan, especially under cathodic potentials. For these reasons, the variation in peak potential with scan rate, given in our previous work [21], should be reconsidered in the light of the present result. Therefore, unless R_s

was proved to be constant, only η_p values obtained for low scan rate were considered relevant. Indeed, under these conditions, the ohmic drop correction did not change the value of E_p, regardless of the R_s value due to small value of I_p.

Variation of cathodic and anodic peak current, I_p (or current density, j_p) with scan rate is illustrated in Fig. 7. The mode of presentation, *i.e.* log ($j_p.v^{-1/2}$) *vs* log ($v^{1/2}$), is the one proposed in [38] to describe the voltammetry response of an insertion compound with a 1D planar geometry (linear diffusion). In such compounds, a transition from a law of the type $I_p \propto v$ to the type $I_p \propto v^{1/2}$ is predicted as the scan rate increases. It is due to the transition from homogeneous diffusion to semi-infinite diffusion as discussed in part 4. The results in Fig. 7 show that I_{pa} was almost equal to I_{pc} at 300°C. At 500°C, I_{pa} was almost equal to I_{pc} only for the high scan rates and lower than I_{pc} at low scan rates. A more detailed study as a function of the temperature would be required to confirm this change in the relative height of anodic and cathodic peaks with temperature. We also noticed from the results in Fig.7 that I_{pc} increased with the temperature. The same was true for I_{pa} for high scan rate, *i.e.* log ($v^{1/2}$) values higher than 0.6. The shape of the variation curve was very similar at both temperatures, *i.e.* I_p increased more significantly with v at the low scan rate. For example, I_{pa} obeyed almost a law of the type $I_p \propto v$ at 500 °C for $v < 50$ mV.s^{-1}. As the scan rate increased, I_p deviated from this variation law to tend towards a law of the type $I_p \propto v^{1/2}$. Typically, at 300 °C, I_p varied almost as $I_p \propto v^{1/2}$ for $v > 10$ mV.s^{-1}. This is important to note that this result must be analyzed with caution because the significant ohmic drop at high scan rate may result in a change in the voltammetry response curve. Indeed, lower peak current may be expected due to uncompensated ohmic drop [50]. The peak potentials, η_{pc} and η_{pa}, measured at 300 and 500 °C as a function of the scan rate were also studied. As previously discussed, we have determined those points where ohmic drop correction makes sense, which leads only to a small number of experimental points that are not represented. From those few points and taking into account the results of impedance measurements [25], we can tentatively propose that η_p did not vary with the scan rate. Indeed, this is consistent with a fast oxygen ion transfer kinetics at the LSCF/GDC interface as evidenced by impedance spectroscopy [25,27,39]. η_{pa} was slightly larger than η_{pc} but

located within the same potential range as expected for an intercalation reaction controlled by mass-transport [40]. The values of η_{pa} and η_{pc} were around -0.35 $V_{/1\ atm}$at 300°C and -0.2 $V_{/1\ atm}$ at 500°C, respectively. As shown in our previous work on the Co-rich LSCF [22], this result confirms that the peak potential was found to increase with the temperature in agreement with the thermodynamic behavior of LSCF [17].

3.2. Role of the oxygen partial pressure

The effect of the oxygen partial pressure was investigated on the porous sample by varying pO_2 from 0.21 to 1.8×10^{-4} atm. Fig. 8a illustrates the cyclic voltammograms obtained at 500 °C under 1.8×10^{-4} atm. Cathodic and reverse anodic peaks were observed similarly to the dense film in air. However, the shape of the voltammogram was more complex and found to vary with the temperature and the scan rate. For temperature lower than 450 °C, only one cathodic peak was observed whatever the scan rate in the range of 0.5 to 80 $mV.s^{-1}$. In the temperature range $450°C \leq T \leq 600°C$, two cathodic peaks could be evidenced. Those peaks were mainly visible at low scan rate as shown in the zoom on Fig. 8a. Double cathodic peaks were also observed by Kournoutis et al. [23] under low oxygen partial pressure at high temperature. At high scan rate, double peaks were hard to identify. However, the cathodic peak exhibited a "complex" shape, different from that obtained for the dense thin film under pO_2 = 0.21 atm. Moreover, the backward anodic peak was always much lower than the forward "complex" cathodic peak. Indeed, the surface area of the anodic peak was approximately 3 to 4 time lower than that of the cathodic peak. At high temperature (T > 600°C), the peaks were not so well defined. Typically, only one large scan rate dependent plateau was observed at 700°C during the forward scan, with a large hysteresis during the reverse scan. The origin of the complex shape of the voltammograms at high temperature is still an open question. Different explanations may be tentatively proposed such as : (i) reversible structural phase transition in LSCF as proposed in [22] for the Co-rich compound, (ii) additional peak due to reduction of oxygen adsorbed species.

Fig. 8b shows the R_s *vs* E curves at different temperatures. Similarly to the dense thin film under air, R_s was found to increase under high cathodic polarization. The higher the temperature, the lower the cathodic polarization necessary to observe R_s enhancement was. In particular at 500 °C, R_s increase was observed even for small cathodic polarization under $pO_2 = 1.8\times10^{-4}$ atm. As already stated, the points above 600°C are not shown in this figure, due to the lack of accurate measurement, which can be seen on the anodic part of the R_s vs E curve at 550°C. However, despite this dispersion, the results obtained at 700°C allowed us to confirm that R_s increase was observed even for small cathodic polarization under $pO_2 = 1.8\times10^{-4}$ atm. In the same way as for the dense film, the overpotential threshold at which R_s was found to increase was calculated. The values obtained were very similar to those obtained with the dense film since we found -0.25 $V_{/1\ atm}$ and -0.13 $V_{/1\ atm}$ at 300 and 500°C, respectively. This good agreement between the two data sets could be an indication that the threshold would be rather fixed by the thermodynamic properties of LSCF. In order, to confirm this interpretation, it would be interesting to examine the effect of changing PO_2 on R_s for the dense film.

The peak currents, I_p (or peak current density, j_p) and peak potentials variation as a function of the scan rate were studied at 300 and 500 °C (Fig. 9a and 9b), for a fixed pO_2 of 1.8×10^{-4} atm. I_{pc} and I_{pa}, were found to increase with the scan rate. At high temperature, the variation law roughly followed the classical $I_p \propto v^{1/2}$ relationship for a semi-infinite linear diffusion as the scan rate increased while it was obtained in all the investigated scan rate range, at 300°C. Indeed, the small deviation at high scan rate observed for I_{pa} as well as the decreasing observed for I_{pc} could be attributed to the ohmic drop effect [50]. The absolute value of I_{pc} was always higher than that of I_{pa}, which could be in agreement with the highest cathodic peak surface area. This was evidenced at 300 °C. Unfortunately, I_{pa} was difficult to be extracted from voltammograms at 500 °C, except for 3 $mV.s^{-1}$ for which $j_{pc} = -2.3\times10^{-3}$ $A.cm^{-2}$ and $j_{pa} = 9\times10^{-4}$ $A.cm^{-2}$, which confirms the above interpretation. As explained from the results in Figure 6, it is likely that the peak potential does not vary with the sweep rate in the whole studied temperature range, since the small increase in potential is not significant. The points reported in Fig. 9b allow us to confirm this interpretation.

This result could be in agreement with fast ion transfer at the GDC/LSCF interface as already discussed for the dense film. Anodic peak potential, η_{pa}, was greater than η_{pc} at 300 °C. The potentials of anodic and cathodic peaks increased with the temperature as already stated.

Fig. 10 compares the polarization curves of the porous film at 500 °C, under $pO_2 = 0.21$ and $pO_2 = 1.8\times10^{-4}$ atm. A few points corresponding to the dc response of the dense film under $pO_2 = 0.21$ atm at 500°C are also indicated. As expected, the steady-state current on the porous film at low pO_2 was lower than at high pO_2 under cathodic polarization. A limiting current was evidenced whose origin is still an open question. Under anodic polarization, the polarization curve was less sensitive on the oxygen partial pressure. As stated in [25], it was mainly attributed to oxygen evolution by the surface path mechanism. At low pO_2, the low value of oxygen reduction rate enabled the peak current due to oxygen transport within LSCF under transient condition to be evidenced on the cyclic voltammetry. A low dc cathodic current was also measured with the thin film under $pO_2 = 0.21$ atm. In that case, it was mainly related to the low specific surface area of the LSCF electrode as shown in Table 1.

4. Discussion

At this stage, the theoretical laws describing the voltammetry response of the oxygen electrode reaction as a function of microstructure in a MIEC have not been established yet. We will, therefore, limit the discussion to a qualitative analysis of the results, based on the theoretical laws established in solution electrochemistry. Indeed, from a formal point of view, it can be suggested that the LSCF/GDC electrode behaves like an oxygen intercalation compound in which oxygen can exchange with the gas phase by a chemical reaction, unlike the insertion compound for which the inserted species is stored only. For those reasons, we will use the theoretical treatments established for the insertion reaction [38] and the EC type reactions (electrochemical reaction followed by a chemical reaction) [37].

4.1. Assignment of peaks

Peaks on the voltammograms can be attributed to de-insertion (cathodic peak) and insertion (anodic peak) of oxygen into LSCF. In terms of defect chemistry, this corresponds to oxygen vacancy transfer at the GDC/LSCF interface and transport by diffusion within LSCF according to the reaction:

$$O_O^x(\text{LSCF}) + V_O^{\cdot\cdot}(\text{GDC}) \leftrightarrow O_O^x(\text{GDC}) + V_O^{\cdot\cdot}(\text{LSCF}) \quad (4)$$

In Eq. (4), the creation of oxygen vacancies within LSCF according to the forward reaction is responsible for the cathodic peak while the anodic peak may be related to their disappearing by the backward reaction. It is worth underlying that reaction (4) corresponds to an electrochemical reaction as described in [26, 42].

In LSCF, it is assumed that there is no barrier for electron transfer [26,32,41,42]. Consequently, the shape of the voltammograms depends on the kinetics of ion transfer and the ion transport rate only. From the η_p variation as a function of the scan rate observed in the present work and according to impedance measurements reported in [25], the kinetics of oxygen ion transfer at the LSCF/GDC interface can be considered as fast so that the electrode potential can be related to the oxygen vacancy ion concentration within LSCF, or oxygen non-stoichiometry, δ, by the so-called insertion isotherm [38,40] or η *vs* δ curve. According to Nernst's equation, the reversible electrode potential, η, can be translated (formally) into an oxygen partial pressure [20,32]. The insertion isotherm is therefore equivalent to the non-stoichiometry curve, δ *vs* ln pO_2, which is fixed by the defect chemistry in the material [16,17]. Consequently, the current responsible for the peak on the voltammetric response, I_{cv}, may be related to the change in oxygen stoichiometry (or oxygen storage capability) according to the relationship [20,38,40]:

$$I_{cv} \propto \frac{d\delta}{d\eta} = \frac{d\delta}{d\,\ln pO_2} \quad (5)$$

From an electrical point of view, it is equivalent to a "capacitive" current, which can be related to the so-called "chemical" capacitance, C_{chem}, determined by impedance spectroscopy. This phenomenon describes the capability of the sample to store chemical energy [32,41,43]. It can be noticed that under thermodynamic control (fast diffusion kinetics) [20,40], the peak current I_p corresponds to the inflection point on the δ *vs* ln pO_2 curve (*i.e.* maximum of $^{d\delta}/_{d\ lnpO_2}$). From a more general point of view, the theoretical response by linear sweep voltammetry of electrochemical insertion reaction is determined from mass-transfer equations, depending on the mass-transfer boundary conditions, using the transfer functions as described in [44].

In LSCF, the insertion reaction (4) is coupled to chemical oxygen exchange reaction at the gas/LSCF interface according to:

$$V_o^{\cdot\cdot}(\mathrm{LSCF}) + \frac{1}{2}O_2 + 2e^- \leftrightarrow O_o^x(\mathrm{LSCF}) \qquad (6)$$

Reaction (6) involves a change of the oxidation state but corresponds to a simple chemical reaction as discussed in [26, 42]. This chemical reaction may modify the shape of the voltammograms in the same way as for an EC reaction [37,45]. According to this interpretation, the main parameter determining the shape of the voltammograms is likely to be the chemical reaction rate, which is directly related to (i) a global surface exchange rate constant, k, depending on the chemistry of the material as defined in [46], (ii) the oxygen partial pressure, pO_2 [47] and (iii) the LSCF specific surface area, S_{MIEC}/gas, which is fixed by the electrode microstructure [39].

4.2. Dependence on the microstructure

We have demonstrated that the shape of the voltammetry response was highly dependent on the LSCF microstructure. From our experimental results, we can suggest that the microstructural parameter, which is likely playing a key role, is the LSCF specific surface area, S_{MIEC}/gas. According to Eq. (1) combined with the f_0 values reported in Table 1, S_{MIEC}/gas can be suggested to be greatly higher for the porous film.

4.2.1 High S_{MIEC}/gas

Thanks to the high specific surface area, the oxygen exchange at the LSCF/gas interface (chemical reaction (6)) is very fast. Under this condition, the extent or penetration depth of the reaction in the electrode must be limited. Both phenomena lead to mitigate the transient accumulation/depletion of oxygen in material. As a consequence, the "hysteresis" or intensity of anodic and cathodic peaks in the voltammogram is very limited for high specific surface area as observed for the SP electrode. Consequently, the voltammetry curve tends towards the polarization curve and the series resistance, R_s, does not vary as a function of the applied potential, as observed experimentally for the LSCF porous film with a fine microstructure under high pO_2.

4.2.2. Low $S_{MIEC/gas}$

At the opposite, the rate of oxygen exchange at the LSCF/gas interface is strongly lowered when the specific surface area is decreased. For a given current density, the reaction has to extend in the depth of the electrode. In these conditions the material is able to store or release oxygen under transient conditions. The "hysteresis" or intensity of peaks is then enhanced for a low specific surface area. Under those conditions, redox peaks attributed to oxygen mass transport within LSCF can be evidenced. Concomitantly, R_s increases under cathodic polarization due to $V_O^{\cdot\cdot}$ concentration profile extending within LSCF. Synchrotron X-Ray studies of model LSCF electrode have shown that chemical expansion due to the creation of $V_O^{\cdot\cdot}$ inside LSCF was higher for LSCF electrode with low specific surface area [48].

It can be noticed that a limiting case, corresponding to no chemical reaction, is the one of an intercalation compound which has been described theoretically [38,40]. Under those conditions, the shape of the voltammograms is highly dependent on the electrode thickness and scan rate. For a thin film or a low scan rate, the cathodic and anodic peaks are rather symmetrical and I_p varies with a law of the type $I_p \propto v$. It can be related to homogeneous diffusion (or finite length diffusion) and thermodynamic reaction rate control, similar to adsorption reaction [38]. For a thick film or high

scan rate, the situation is equivalent to the classical response of a fast redox system with a kinetics governed by semi-infinite diffusion, like in solution electrochemistry [37,38]. It is characterized by a variation of I_p according to $I_p \propto v^{1/2}$. In both cases, E_{pc} and E_{pa} are independent of the scan rate. This behavior could correspond to that observed experimentally for the dense thin film under air. In conclusion, although LSCF cannot be strictly considered as an insertion compound due to the fact that the oxygen intercalation process is coupled with chemical oxygen exchange with the gas phase, it can be tentatively proposed that a transition from homogeneous diffusion of oxygen ions to semi-infinite diffusion is evidenced in the dense LSCF thin film under air. This transition shifts to higher scan rate as the temperature increases due to increasing the oxygen diffusion coefficient with the temperature.

4.2.3. Medium $S_{MIEC/gas}$

For intermediate specific surface areas, the shape of the voltammograms is expected to be a combination of both limiting situations depicted previously, *i.e.* steady-state current and redox peak superimposed as shown in EC mechanism [37]. For example, the voltammetry response could not correspond to the polarization curve without clearly evidencing the redox peaks. This situation could be the one encountered in the work of Kournoutis et al. [23] for the response of porous $La_{0.8}Sr_{0.2}Co_{0..2}Fe_{0.8}O_{3-\delta}$ under air. Indeed, in this work, the oxygen exchange rate at the gas/MIEC interface is expected to be in between both limiting cases described above, due to the likely less important specific surface area (higher sintering temperature) in addition to lowest Sr content. This intermediate oxygen exchange rate could lead to small variation of R_s with the dc cathodic potential and negligible peak currents. The small variation of R_s could be at the origin of the inverse hysteresis phenomenon observed in their work [23] and in an old work of one of the authors on LSM [49].

In order to confirm this assumption, we have tested a porous thick sample with a columnar microstructure. The film was 34 µm thick, consisting of columns with a large amount of nanostructured porosity, with approximately 1 µm gaps visible throughout the surface as shown in

Fig. 3 (e) and (f). In this sample, the LSCF specific surface area corresponded mainly to the surface area of the column walls as well as some open nanoporosity inside the columns. Therefore, it was expected to be lower than that of the porous SP LSCF film. The specific surface area variation was roughly estimated from the f_0 frequency shift given in Table 1. We found that the specific surface area for the columnar film was almost 13 times lower than that of the porous film. The voltammogram and R_s *vs* E curve measured at 300 °C under pO_2 = 0.21 atm for the columnar film are represented in Fig. 11a and 11b, respectively. R_s was found to slightly increase with the dc cathodic bias, probably because of a poor vacancies extension in the MIEC. It is worth noting that R_s was more important than that corresponding to the GDC electrolyte resistance. This could be attributed to in-plane resistance of the columnar microstructure, leading to constriction within LSCF. The reverse hysteresis was evidenced on the voltammograms. This phenomenon could be tentatively related to small R_s variation. Indeed, during the forward scan R_s increases with the cathodic polarization. Then, the E(j) curve shifted to the left although the opposite might occur during the reverse scan, with an E(j) curve shift to the right. For instance, the variation of R_s, ΔR_s, estimated from the shift on the right at j = -2.0×10^{-3} A.cm^{-2} was equal to 10.7 Ω.cm^{-2}, which is compatible with the variation of R_s in Fig. 11b. This phenomenon could be tentatively proposed as being at the origin of the reverse hysteresis.

4.3. Dependence on pO_2

The experimental results obtained on the 10 µm porous LSCF layer have demonstrated that by decreasing pO_2 from 0.21 to 1.8×10^{-4}, the shape of the voltammograms changes from the polarization curve to an E(j) transient response, corresponding to a fast redox system with a kinetics limited by semi-infinite linear diffusion (E_p = constant and $I_p \propto v^{1/2}$) coupled with a chemical reaction leading to the steady-rate current [37,45]. Here again, it can be explained in terms of slow kinetics of reaction (6). Indeed, decreasing pO_2 leads to decrease the rate of oxygen adsorption and

incorporation in LSCF. This allows highest penetration of $V_o^{\cdot\cdot}$ inside LSCF. Consequently, redox peaks related to $V_o^{\cdot\cdot}$ diffusion are observed and concomitantly R_s increases as the applied potential becomes more negative. This result is in agreement with in-situ high-temperature XRD experiment performed by Kivi et al. [15], which shows that pO_2 has a noticeable and reversible influence on the crystallographic cell volume increase under polarization. The return peak is expected to highly depend on the value of k. The higher the value of the surface exchange rate k, the lower the surface area of the return peak. This is in agreement with our experimental results (see Fig. 9), which show that I_{pa} was always lower than I_{pc}.

4.4. Limitation of voltammetry

One of the interests of voltammetry is that it allows studying a material in a large potential and time-scale domain. However, a major problem with this technique is the ohmic drop. Indeed, uncompensated ohmic resistance introduces an additional term in the expression for the applied potential (see Eq. (2)), which results in a distortion of the voltammograms [50]. Most of the electrochemical apparatus enable iR compensation. However, this correction is possible only if R_s is a constant.

In the present work, we have evidenced that R_s may vary with the applied cathodic potential for the LSCF/GDC electrode. It results that iR drop compensation may be almost impossible to be achieved properly. So, the conditions assumed in the theoretical analysis would be difficult to be met in practice thus complicating quantitative analysis. With a small amplitude signal, the electrode behavior is nearly linear, so electrode impedance measurements should provide correct value of R_s for every electrode potential.

5. Conclusion

The electrode microstructure plays a key role on the shape of the voltammograms of the LSCF/GDC electrode under air at a high temperature as well as on the high-frequency series resistance, R_s, variation with the dc potential.

For a porous film with a fine microstructure, the voltammograms were identical to the polarization curve and R_s did not vary with the applied potential. Those results were interpreted in terms of high LSCF specific surface area, leading to fast kinetics of the oxygen exchange chemical reaction at the LSCF/gas interface. This situation was proposed to correspond to that of an EC mechanism with a fast chemical reaction rate.

For a LSCF film with a low specific surface area (dense LSCF), the voltammograms were found to be almost similar to those of an intercalation compound with symmetrical cathodic and anodic peaks. Concomitantly, R_s was found to increase under cathodic dc bias. Those results were attributed to oxygen stoichiometry change within LSCF, due to oxygen vacancy transfer at the LSCF/GDC interface and transport by diffusion within LSCF, followed by a slow oxygen chemical exchange rate at the LSCF/gas interface.

The oxygen partial pressure greatly affects the voltammetry response. Here again, the results were interpreted in terms of the oxygen chemical exchange rate at the LSCF/gas interface, which decreases as pO_2 decreases.

The limitation of the voltammetry for the study of the LSCF/GDC electrode due to possible R_s variation was highlighted. This phenomenon could be tentatively proposed as being at the origin of the reverse hysteresis observed sometimes on the voltammetry response.

Acknowledgements

This work was financially supported by the Institute of Engineering Univ. Grenoble Alpes (AGIR-POLE 2016). The authors would like to thank Dr C. Montella (LEPMI, Univ. Grenoble Alpes) for fruitful discussions on electrochemical kinetics and Dr F. Charlot (CMTC, Univ. Grenoble Alpes) for making the SEM observations.

References

[1] S.J. Skinner, Recent advances in Perovskite-type materials for solid oxide fuel cell cathodes, Int. J. Inorg. Mater. 3 (2001) 113–121. doi:10.1016/S1466-6049(01)00004-6.

[2] L.W. Tai, M.M. Nasrallah, H.U. Anderson, D.M. Sparlin, S.R. Sehlin, Structure and electrical properties of $La_{1-x}Sr_xCo_{1-y}Fe_yO_3$. Part 2. The system $La_{1-x}Sr_xCo_{0.2}Fe_{0.8}O_3$, Solid State Ionics. 76 (1995) 273–283. doi:10.1016/0167-2738(94)00245-N.

[3] B. Fan, J. Yan, X. Yan, The ionic conductivity, thermal expansion behavior, and chemical compatibility of $La_{0.54}Sr_{0.44}Co_{0.2}Fe_{0.8}O_{3-\delta}$ as SOFC cathode material, Solid State Sci. 13 (2011) 1835–1839. doi:10.1016/j.solidstatesciences.2011.07.007.

[4] S.P. Jiang, A comparison of O_2 reduction reactions on porous (La,Sr)MnO3 and (La,Sr)(Co,Fe)O_3 electrodes, Solid State Ionics. 146 (2002) 1–22. doi:10.1016/S0167-2738(01)00997-3.

[5] K. Murata, T. Fukui, H. Abe, M. Naito, K. Nogi, Morphology control of La(Sr)Fe(Co)$O_{3-\delta}$ cathodes for IT-SOFCs, J. Power Sources. 145 (2005) 257–261. doi:10.1016/j.jpowsour.2004.12.063.

[6] L. Baqué, A. Caneiro, M.S. Moreno, A. Serquis, High performance nanostructured IT-SOFC cathodes prepared by novel chemical method, Electrochem. Commun. 10 (2008) 1905–1908. doi:10.1016/j.elecom.2008.10.010.

[7] Ö. Çelikbilek, E. Siebert, D. Jauffrès, C.L. Martin, E. Djurado, Influence of sintering temperature on morphology and electrochemical performance of LSCF/GDC composite films as efficient cathode for SOFC, Electrochim. Acta. 246 (2017) 1248–1258. doi:10.1016/j.electacta.2017.06.070.

[8] D. Marinha, L. Dessemond, E. Djurado, Microstructure-Electrical Properties of Original LSCF Films Deposited by ESD for IT-SOFCs, ECS Trans. . 28 (2010) 93–103. doi:10.1149/1.3495835.

[9] H.J. Hwang, J.W. Moon, S. Lee, E.A. Lee, Electrochemical performance of LSCF-based composite cathodes for intermediate temperature SOFCs, J. Power Sources. 145 (2005) 243–248. doi:10.1016/j.jpowsour.2005.02.063.

[10] D. Marinha, L. Dessemond, J.S. Cronin, J.R. Wilson, S.A. Barnett, E. Djurado, Microstructural 3D reconstruction and performance evaluation of LSCF cathodes obtained by electrostatic spray deposition, Chem. Mater. 23 (2011) 5340–5348. doi:10.1021/cm2016998.

[11] H.. Tu, Y. Takeda, N. Imanishi, O. Yamamoto, $Ln_{0.4}Sr_{0.6}Co_{0.8}Fe_{0.2}O_{3-\delta}$ (Ln=La, Pr, Nd, Sm, Gd) for the electrode in solid oxide fuel cells, Solid State Ionics. 117 (1999) 277–281. doi:10.1016/S0167-2738(98)00428-7.

[12] V. V. Kharton, F. Figueiredo, L. Navarro, E. Naumovich, A. Kovalevsky, A. Yaremchenko, A. Viskup, A. Carneiro, F. Marques, J. Frade, Ceria-based materials for solid oxide fuel cells, J. Mater. Sci. 36 (2001) 1105–1117. doi:10.1023/A:1004817506146.

[13] R. Kiebach, W. Zhang, M. Chen, K. Norrman, H.J. Wang, J.R. Bowen, R. Barfod, P.V. Hendriksen, W. Zhang, Stability of $La_{0.6}Sr_{0.4}Co_{0.2}Fe_{0.8}O_3/Ce_{0.9}Gd_{0.1}O_2$ cathodes during sintering and solid oxide fuel cell operation, J. Power Sources. 283 (2015) 151–161. doi:10.1016/j.jpowsour.2015.02.064.

[14] E. Bucher, W. Sitte, G.B. Caraman, V.A. Cherepanov, T. V. Aksenova, M. V. Ananyev, Defect equilibria and partial molar properties of $(La,Sr)(Co,Fe)O_{3-\delta}$, Solid State Ionics. 177 (2006) 3109–3115. doi:10.1016/j.ssi.2006.07.062.

[15] I. Kivi, J. Aruvali, K. Kirsimae, A. Heinsaar, G. Nurk, E. Lust, Oxygen Stoichiometry in $La_{0.6}Sr_{0.4}CoO_{3-\delta}$ and $La_{0.6}Sr_{0.4}Co_{0.2}Fe_{0.8}O_{3-\delta}$ Cathodes under Applied Potential as a Function of Temperature and Oxygen Partial Pressure, Measured by Electrochemical in Situ High-Temperature XRD Method, J. Electrochem. Soc. 160 (2013) F1022–F1026. doi:10.1149/2.072309jes.

[16] S.I. Hashimoto, Y. Fukuda, M. Kuhn, K. Sato, K. Yashiro, J. Mizusaki, Oxygen nonstoichiometry and thermo-chemical stability of $La_{0.6}Sr_{0.4}Co_{1-y}Fe_yO_{3-\delta}$ (y = 0.2, 0.4, 0.6, 0.8), Solid State Ionics. 181 (2010) 1713–1719. doi:10.1016/j.ssi.2010.09.024.

[17] M. Kuhn, Y. Fukuda, S. Hashimoto, K. Sato, K. Yashiro, J. Mizusaki, Oxygen nonstoichiometry and thermo-chemical stability of perovskite-type $La_{0.6}Sr_{0.4}Co_{1-y}Fe_yO_{3-\delta}$ (y = 0, 0.2, 0.4, 0.5, 0.6, 0.8, 1) materials, J. Electrochem. Soc. 160 (2013) 34–42. doi:10.1149/2.050301jes.

[18] X.J. Chen, S.H. Chan, K.A. Khor, Cyclic voltammetry of (La,Sr)MnO_3 electrode on YSZ substrate, Solid State Ionics. 164 (2003) 17–25. doi:10.1016/j.ssi.2003.08.006.

[19] V. Roche, A. Hadjar, J.P. Deloume, T. Pagnier, R. Revel, C. Roux, E. Siebert, P. Vernoux, Physicochemical origins of electrochemical promotion of LSM/YSZ, Catal. Today. 146 (2009) 266–273. doi:10.1016/j.cattod.2009.03.031.

[20] J. Van Herle, S. Diethelm, Electrochemical characterisation of oxygen nonstoichiometry and transport in mixed conducting oxidesApplication to $La_{0.4}Ba_{0.6}Fe_{0.8}Co_{0.2}O_{3-\delta}$, Solid State Ionics. 174 (2004) 127–134. doi:10.1016/j.ssi.2004.07.028.

[21] E. Siebert, C. Roux, A. Boréave, F. Gaillard, P. Vernoux, Oxido-reduction properties of $La_{0.7}Sr_{0.3}Co_{0.8}Fe_{0.2}O_{3-\delta}$ perovskite oxide catalyst, Solid State Ionics. 183 (2011) 40–47. doi:10.1016/j.ssi.2010.11.012.

[22] E. Siebert, A. Boréave, F. Gaillard, T. Pagnier, Electrochemical and Raman study of $La_{0.7}Sr_{0.3}Co_{0.8}Fe_{0.2}O_{3-\delta}$ reduction, Solid State Ionics. 247–248 (2013) 30–40. doi:10.1016/j.ssi.2013.05.006.

[23] V.C. Kournoutis, F. Tietz, S. Bebelis, Cyclic voltammetry characterization of a $La_{0.8}Sr_{0.2}Co_{0.2}Fe_{0.8}O_{3-\delta}$ electrode interfaced to CGO/YSZ, Solid State Ionics. 197 (2011) 13–17. doi:10.1016/j.ssi.2011.06.007.

[24] J. Rutman, I. Riess, Reference electrodes for thin-film solid-state ionic devices, Solid State Ionics. 179 (2008) 108–112. doi:10.1016/j.ssi.2007.12.040.

[25] J.L. Federico Monaco, V. Tezyk, E. Siebert, S. Pylypko, B. Morel, J. Vulliet, T. Le Bigan, F. Lefebvre-Joud, Experimental validation of a $La_{0.6}Sr_{0.4}Co_{0.2}Fe_{0.8}O_{3-\delta}$ electrode model operated in electrolysis mode: Understanding the reaction pathway under anodic polarization., Solid State Ionics. 319 (2018) 234 - 246. doi: 10.1016/j.ssi.2018.02.012.

[26] S.B. Adler, Electrode Kinetics of Porous Mixed-Conducting Oxygen Electrodes, J. Electrochem. Soc. 143 (1996) 3554. doi:10.1149/1.1837252.

[27] J. Nielsen, T. Jacobsen, M. Wandel, Impedance of porous IT-SOFC LSCF:CGO composite cathodes, Electrochim. Acta. 56 (2011) 7963–7974. doi:10.1016/j.electacta.2011.05.042.

[28] J. Nielsen, P. Hjalmarsson, M.H. Hansen, P. Blennow, Effect of low temperature in-situ sintering on the impedance and the performance of intermediate temperature solid oxide fuel cell cathodes, J. Power Sources. 245 (2014) 418–428. doi:DOI 10.1016/j.jpowsour.2013.06.067.

[29] B.C.H. Steele, Appraisal of $Ce_{1-y}Gd_yO_{2-y}$ / 2 electrolytes for IT-SOFC operation at 500C, Solid State Ionics. 129 (2000) 95–110.

[30] M. Kleitz, F. Petitbon, Optimized SOFC electrode microstructure, Solid State Ionics. 92 (1996) 65–74. doi:10.1016/S0167-2738(96)00464-X.

[31] N. Hildenbrand, B.A. Boukamp, P. Nammensma, D.H.A. Blank, Improved cathode/electrolyte interface of SOFC, Solid State Ionics. 192 (2011) 12–15. doi:10.1016/j.ssi.2010.01.028.

[32] F.S. Baumann, J. Fleig, H.U. Habermeier, J. Maier, Impedance spectroscopic study on well-defined (La,Sr)(Co,Fe)$O_{3-\delta}$ model electrodes, Solid State Ionics. 177 (2006) 1071–1081. doi:10.1016/j.ssi.2006.02.045.

[33] C. Niedrig, S.F. Wagner, W. Menesklou, E. Ivers-Tiffee, Characterization of oxygen-dependent stability of selected mixed-conducting perovskite oxides, Solid State Ionics. 273 (2015) 41–45. doi:10.1016/j.ssi.2014.12.008.

[34] J. Fleig, The Influence of Current Constriction on the Impedance of Polarizable Electrodes, J. Electrochem. Soc. 144 (1997) L302. doi:10.1149/1.1838076.

[35] T. Kenjo, Y. Kanehira, Influence of the local variation of the polarization resistance on SOFC cathodes, Solid State Ionics. 148 (2002) 1–14. doi:10.1016/S0167-2738(02)00119-4.

[36] O. Celikbilek, L. Dessemond, E. Djurado, State-of-the-Art $La_{0.6}Sr_{0.4}Co_{0.2}Fe_{0.8}O_{3-\delta}$ Cathode for SOFC: Microstructural and Electrochemical Properties, ECS Trans. 78 (2017) 747–758.

doi:10.1149/07801.0747ecst.

[37] A. Bard, L. Faulkner, Electrochemical Methods: Fundamentals and Applications, 2001, Wiley. doi:10.1016/B978-0-12-381373-2.00056-9.

[38] J.-P. Diard, B. Le Gorrec, Claude Montella, Cinetique électrochimique, Hermann, Paris, 1996.

[39] M. Hubert, J. Laurencin, P. Cloetens, J.C. da Silva, F. Lefebvre-Joud, P. Bleuet, A. Nakajo, E. Siebert, Role of microstructure on electrode operating mechanisms for mixed ionic electronic conductors: From synchrotron-based 3D reconstruction to electrochemical modeling, Solid State Ionics. 294 (2016) 90–107. doi:10.1016/j.ssi.2016.07.001.

[40] S.Y. Vassiliev, E.E. Levin, V.A. Nikitina, Kinetic analysis of lithium intercalating systems: Cyclic voltammetry, Electrochim. Acta. 190 (2016) 1087–1099. doi:10.1016/j.electacta.2015.12.172.

[41] T. Kawada, J. Suzuki, M. Sase, A. Kaimai, K. Yashiro, Y. Nigara, J. Mizusaki, K. Kawamura, H. Yugami, Determination of Oxygen Vacancy Concentration in a Thin Film of $La_{0.6}Sr_{0.4}CoO_{3-\delta}$ by an Electrochemical Method, J. Electrochem. Soc. 149 (2002) E252. doi:10.1149/1.1479728.

[42] J. Laurencin, M. Hubert, K. Couturier, T. Le Bihan, P. Cloetens, F. Lefebvre-Joud, E. Siebert, Reactive Mechanisms of LSCF Single-Phase and LSCF-CGO Composite Electrodes Operated in Anodic and Cathodic Polarisations, Electrochim. Acta. 174 (2015) 1299–1316. doi:10.1016/j.electacta.2015.06.080.

[43] J. Jamnik, J. Maier, S. Pejovnik, A powerful electrical network model for the impedance of mixed conductors, Electrochim. Acta. 44 (1999) 4139–4145. doi:http://dx.doi.org/10.1016/S0013-4686(99)00128-0.

[44] F. Berthier, J.-P. Diard, C. Montella, Numerical solution of coupled systems of ordinary and partial differential equations. Application to the study of electrochemical insertion reactions by linear sweep voltammetry, J. Electroanal. Chem. 502 (2001). doi:10.1016/S0022-0728(00)00544-1.

[45] H. Girault, Electrochimie physique et Analytique, Presses Polytechniques et Universitaires Romandes, Lausanne, 2001.

[46] J. Maier, On the correlation of macroscopic and microscopic rate constants in solid state chemistry, Solid State Ionics. 112 (1998) 197–228. doi:10.1016/S0167-2738(98)00152-0.

[47] Y. Li, K. Gerdes, T. Horita, X. Liu, Surface Exchange and Bulk Diffusivity of LSCF as SOFC Cathode: Electrical Conductivity Relaxation and Isotope Exchange Characterizations, J. Electrochem. Soc. 160 (2013) F343–F350. doi:10.1149/2.044304jes.

[48] K.C. Chang, B. Ingram, J. Ilavsky, S. Lee, P. Fuoss, H. You, Synchrotron X-ray studies of model SOFC cathodes, part I: Thin film cathodes, Solid State Ionics. 311 (2017) 118–126. doi:10.1016/j.ssi.2017.10.005.

[49] A. Hammouche, A. Caneiro, E. Siebert, A. Hammou, M. Kleitz, Electrocatalytique properties and nonstoichiometry of the high temperature air electrode, J. Electrochem. Soc. 138 (1991) 1212-1216

[50] http://www.bio-logic.info, Application note 27, Ohmic drop correction. I Effect on measurements

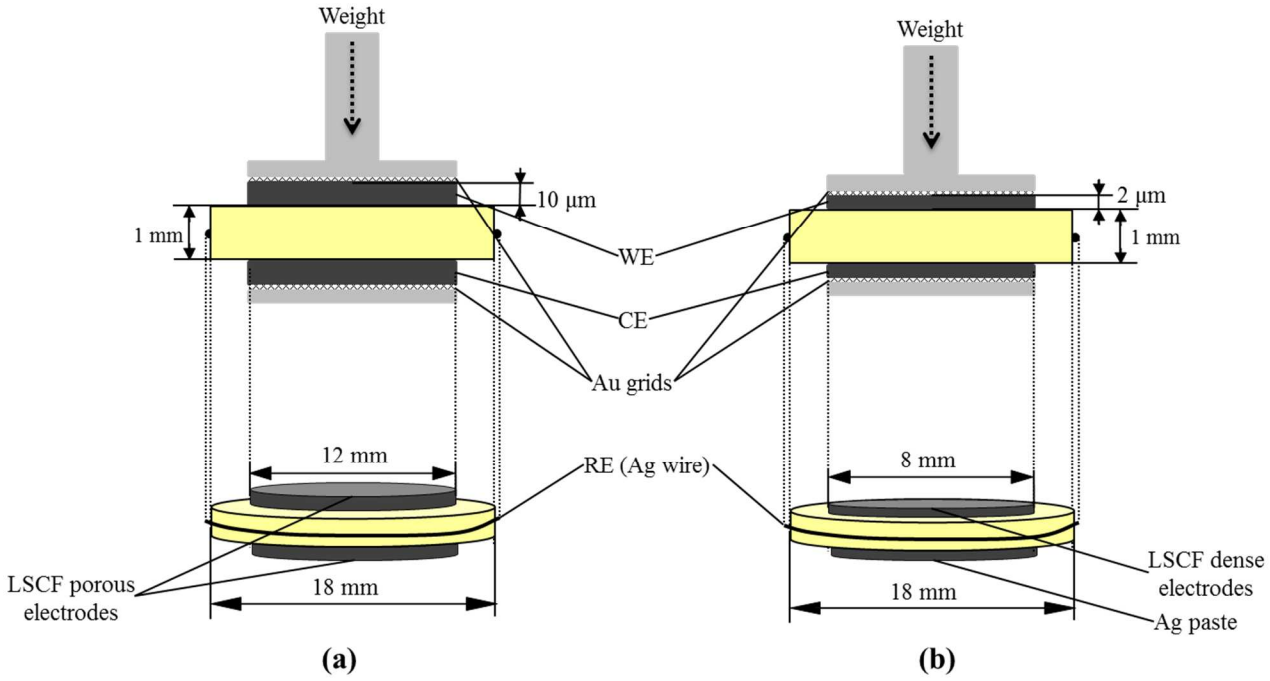

Figure 1

Fig.1. Description of the three-electrode set-up. Cell dimensions and nature of the electrodes for tests with porous LSCF (a) and dense LSCF (b).

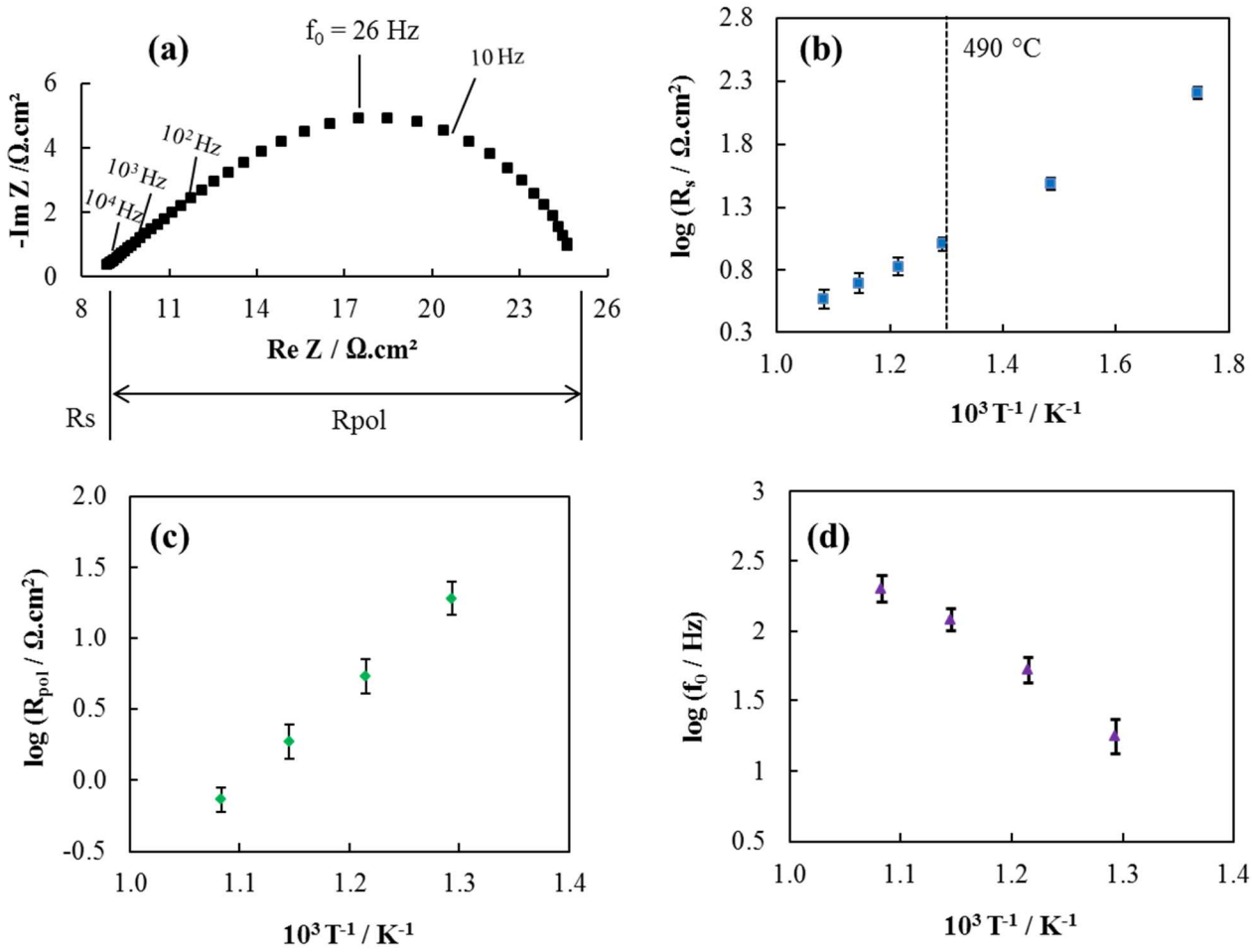

Figure 2

Fig.2. (a) Typical impedance spectrum at OCV (pO_2 = 0.21 atm, T = 500 °C). Arrhenius plot of (b) R_s, (c) R_{pol} and (d) f_0. The error was estimated from 4 similar porous films deposited on GDC.

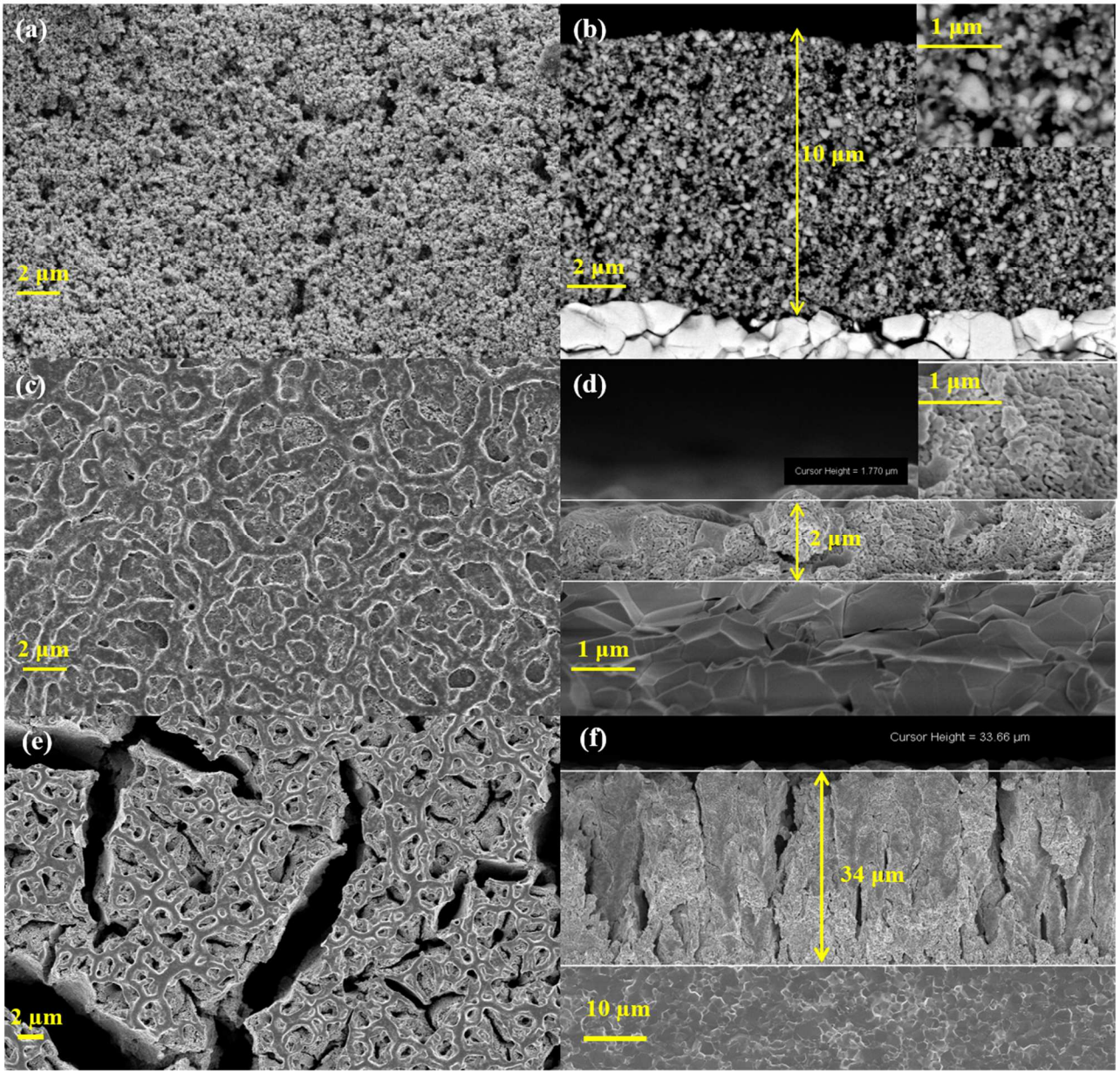

Figure 3

Fig.3. SEM images of the surface (on the left) and the cross-section (on the right) for the different LSCF electrodes. (a) and (b) SP porous sample. (c) and (d) ESD almost dense sample. (e) and (f) ESD columnar sample

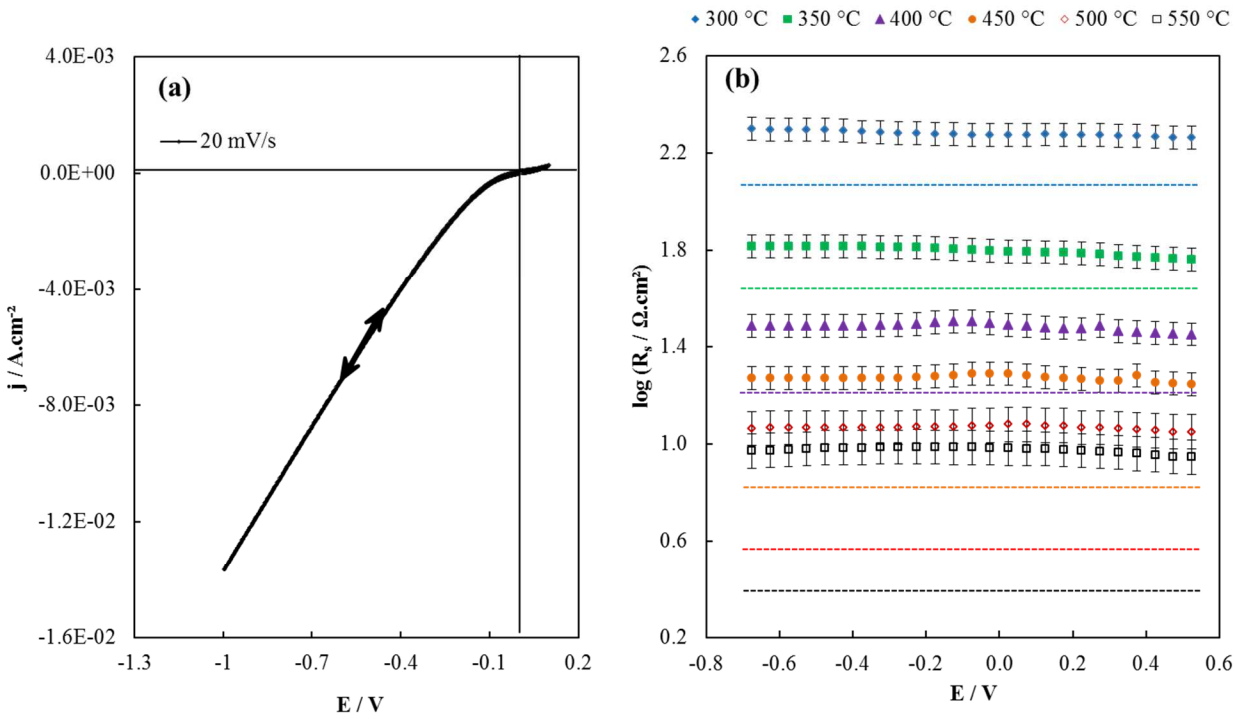

Figure 4

Fig. 4. Typical electrochemical measurements for the porous LSCF electrode under pO_2 = 0.21 atm. (a) Cyclic voltammetry (pre-treatment 0.1 V for 600 s, T = 407 °C). (b) R_s dependence on applied dc potential (E) for different temperatures. For comparison R_s^{GDC} calculated from Steele's data [29] at the same temperatures is represented by the dashed lines.

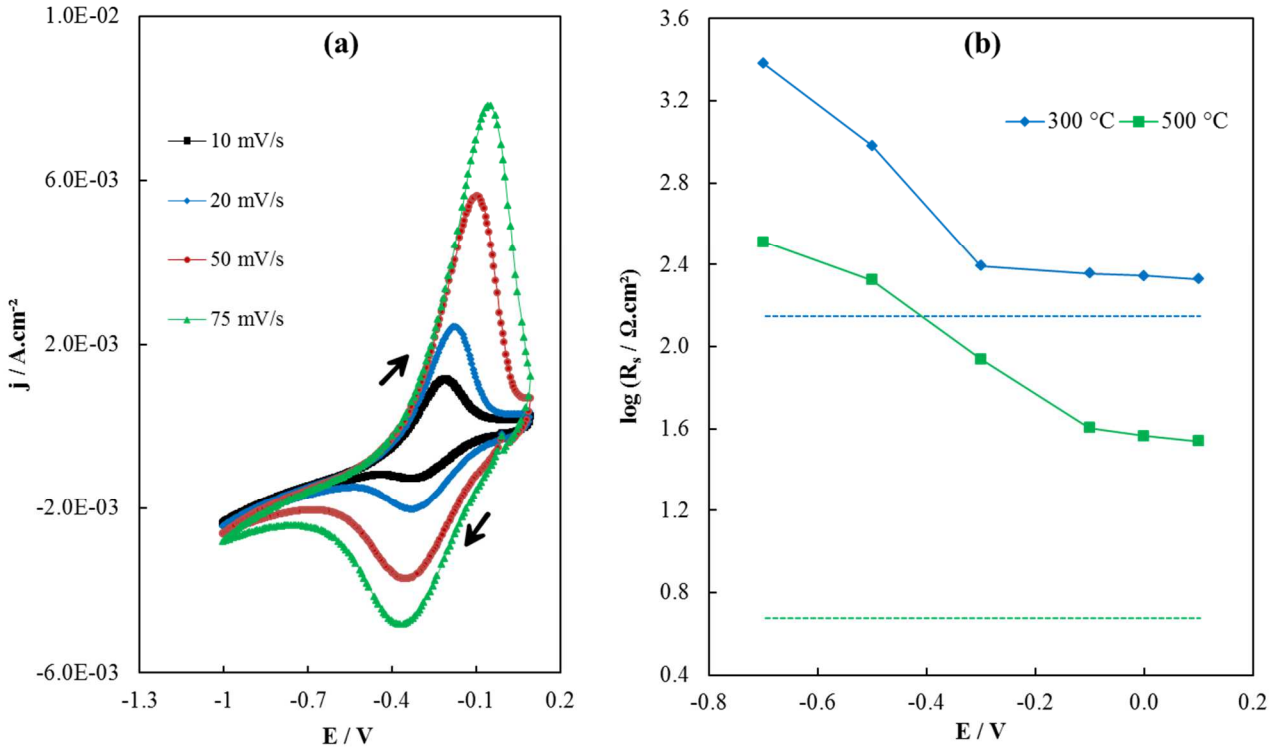

Figure 5

Fig. 5. Typical electrochemical measurements for the dense LSCF electrode under pO_2 = 0.21 atm. (a) Cyclic voltammetry (pre-treatment 0.1 V for 600 s, T = 500 °C). (b) R_s dependence on applied dc potential (E). For comparison Rs^{GDC} calculated from Steele's data [29] at 300 °C and 500 °C is represented by the dashed lines.

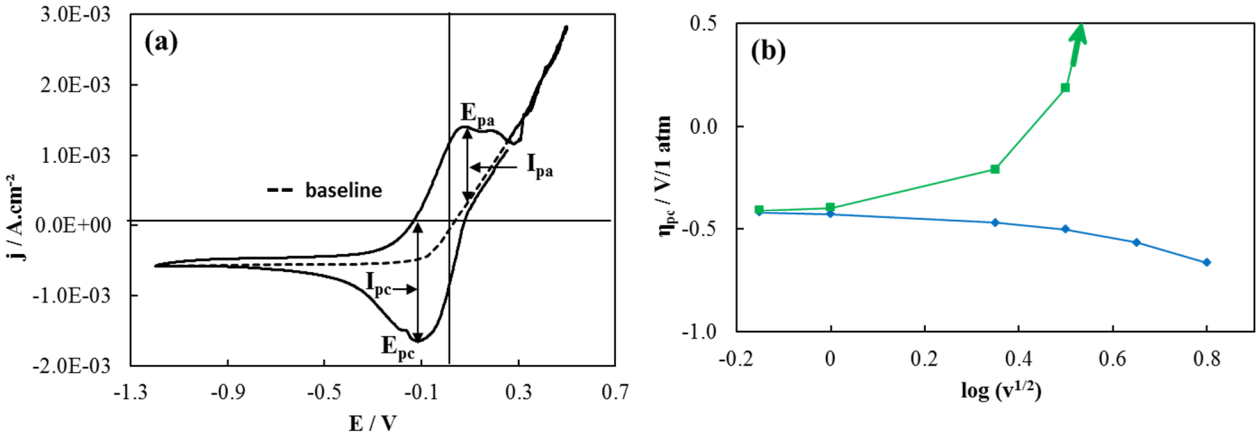

Figure 6

Fig. 6. (a) Peak current and peak potential determination mode. (b) Peak potential, η_p, determined according to Eq. (1) with $R_s = R_s(OCV)$ (blue) or $R_s = R_s(E)$ (green). The determination mode is illustrated on the cathodic peak at 300 °C. The green arrow indicates a large increase in η_{pc}.

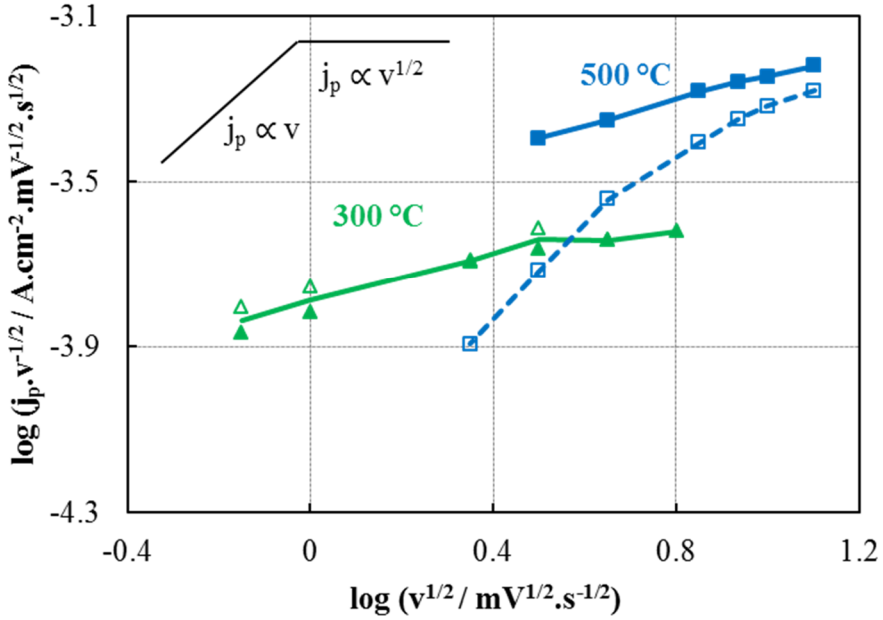

Figure 7

Fig. 7. Variation of the voltammetry parameters as a function of the scan rate for the dense film under pO_2 = 0.21 atm. j_{pc} (filled symbol) and j_{pa} (empty symbol) at 300 °C (green) and 500 °C (blue). The line is only a guide for the eyes. The representation mode is the one proposed by Diard et al. [38].

.

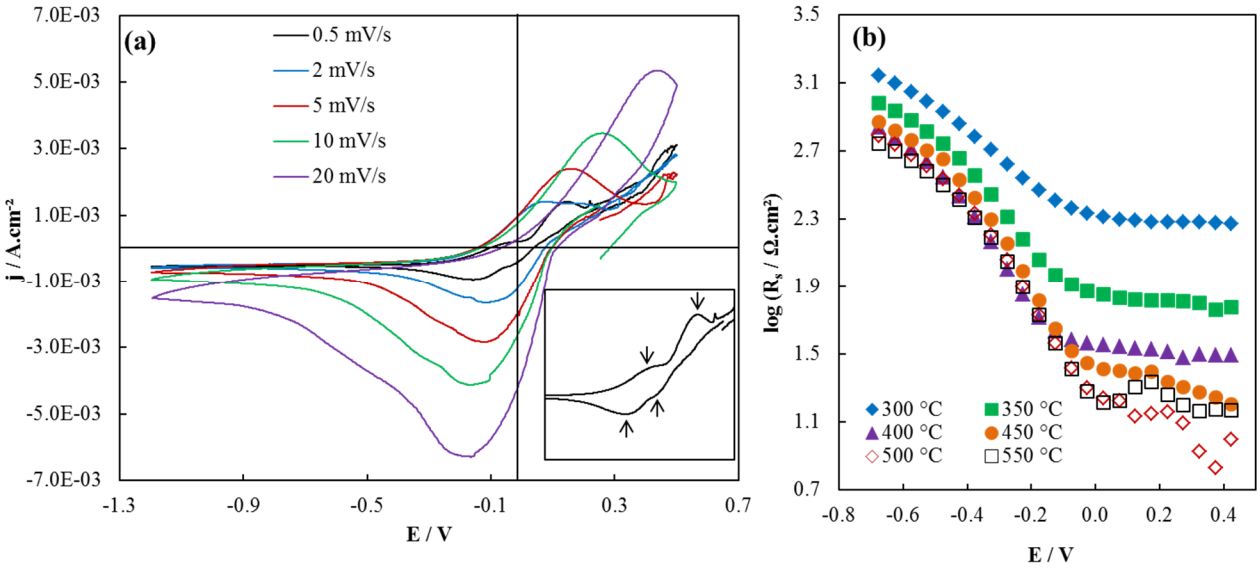

Figure 8

Fig. 8. Typical electrochemical measurements for the porous LSCF electrode under $pO_2 = 1.8\times10^{-4}$ atm. (a) Cyclic voltammetry (pre-treatment 0.25 V for 600 s, T = 500°C). The insert shows a zoom of the voltammetry curve at 0.5 $mV.s^{-1}$. (b) R_s dependence on applied dc potential (E) for different temperatures.

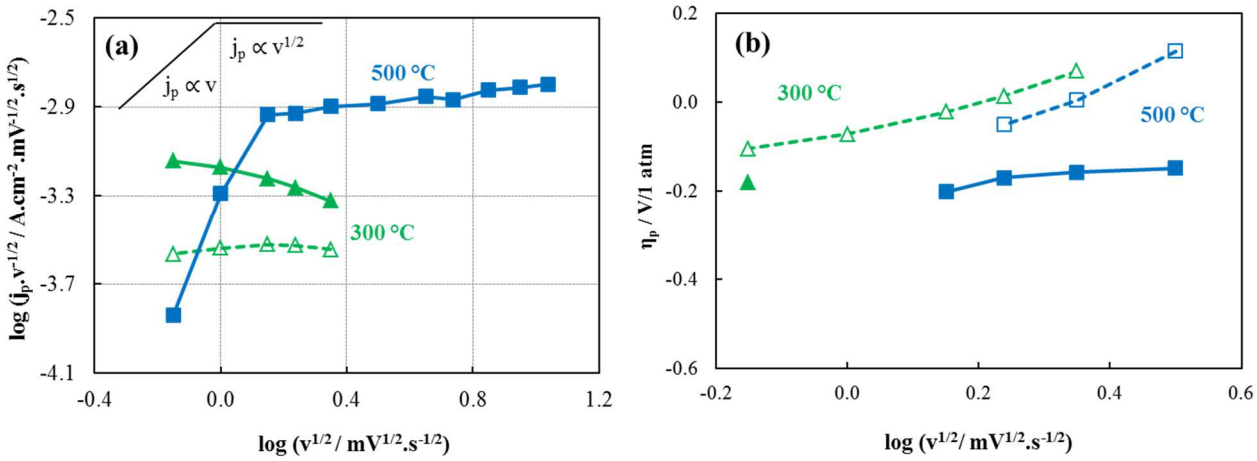

Figure 9

Fig. 9. Variation of the voltammetry parameters as a function of the scan rate for the porous film under $pO_2 = 1.8\times10^{-4}$ atm. (a) j_{pc} (filled symbol) and j_{pa} (empty symbol) at 300 °C (green) and j_{pc} at 500 °C (blue). The line is only a guide for the eyes. (b) η_{pa} (empty symbol) and η_{pc} (filled symbol) at 300 °C (green) and at 500 °C (blue). The representation mode is the one proposed by Diard et al. [38].

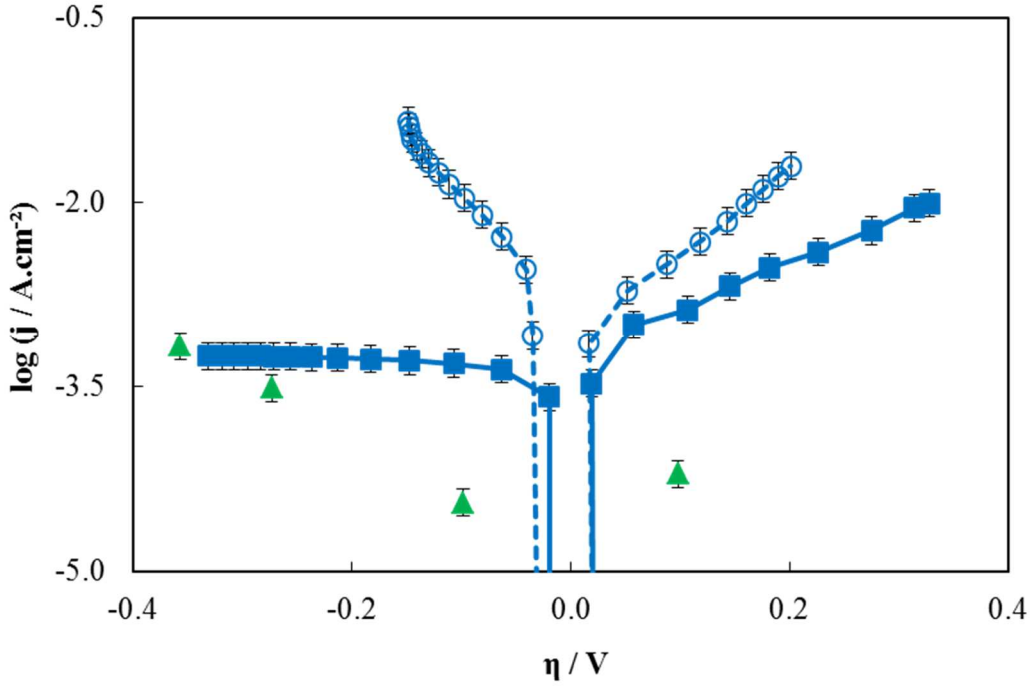

Figure 10

Fig. 10. Comparison of the polarization curves of the porous thick film (blue) under pO_2 = 0.21 atm (empty symbol) and $pO_2 = 1.8\times10^{-4}$ atm (filled symbol) at 500 °C. A few points corresponding to the log (j) *vs* η curve for the dense thin film (green) are indicated (T = 500 °C, pO_2 = 0.21 atm).

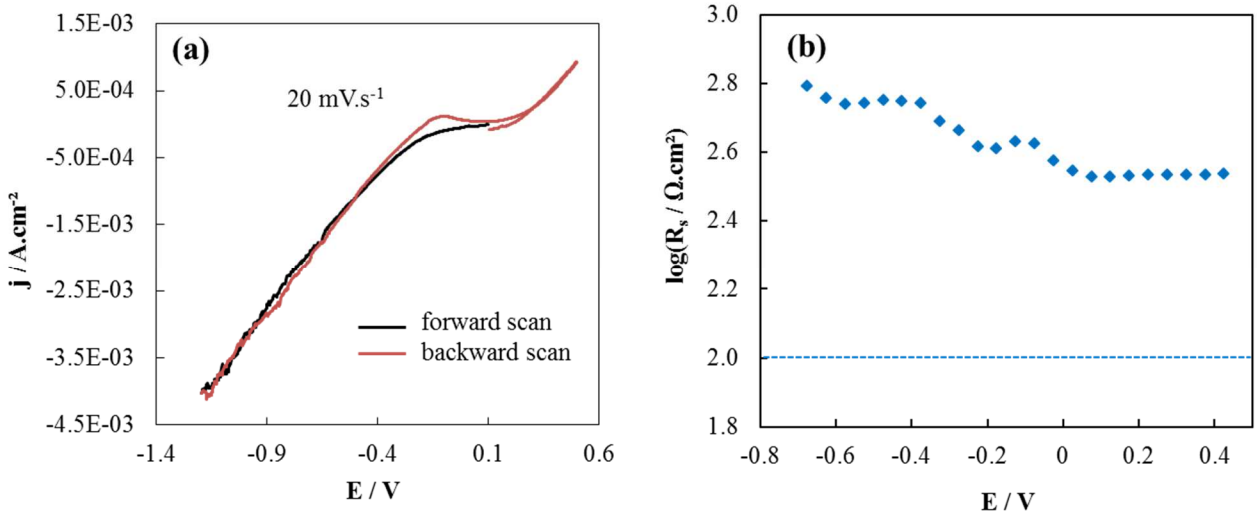

Figure 11

Fig. 11. Electrochemical measurements for the columnar LSCF electrode under pO_2 = 0.21 atm at T= 300°C. (a) Cyclic voltammetry (pre-treatment 0.1 V for 600 s). (b) R_s dependence on applied dc potential (E). For comparison R_s^{GDC} calculated from Steele's data [29] is represented by the dashed line.